

# Spatially Resolved Dynamically Reconfigurable Multilevel Control of Thermal Emission

Ziquan Xu, Qiang Li,\* Kaikai Du, Shiwei Long, Yang Yang, Xun Cao, Hao Luo, Huanzheng Zhu, Pintu Ghosh, Weidong Shen, and Min Qiu

Spatially resolved dynamically reconfigurable control of thermal emission has comprehensive implications for fundamental science and technological applications, such as thermal camouflage and adaptive radiative heating/cooling. Materials and systems that can spatially control thermal emission with dynamic reconfigurability, simple manufacturability, and a large dynamic range have not been explored, so far. Here, a spatially resolved thermal emission control platform consisting of three components (a VO<sub>2</sub> material with phase transition hysteresis, a thermal photonic device with a field-optimized planarized structure, and an optically controllable patterning system) is built and validated. This platform presents excellent merits such as spatially resolved control of thermal emission, multilevel (up to nine levels) emission control with a large dynamic range of the emissivity modulation (0.19 for the insulating phase and 0.91 for the metallic phase) over a broad bandwidth (8–14 μm), and robust reconfigurability. The results demonstrate potential applications in the field of thermal photonics for information and energy harvesting.

## 1. Introduction

Control over the thermal emission of a thermal photonic device is fundamental to its application in energy-harvesting and information fields, including thermal management (radiative heating/cooling<sup>[1–5]</sup> and thermophotovoltaics<sup>[6–8]</sup>), molecular sensing,<sup>[9,10]</sup> thermal infrared (IR) sources,<sup>[11–16]</sup> and thermal camouflage.<sup>[17–20]</sup> Thermal emission, which is radiative electromagnetic energy outflow due to the thermal motion of charged particles, is determined by Planck's law of black-body radiation. For switchable spectral control of thermal emission, devices that integrate the intrinsic electrical/optical/thermal properties of materials such as semiconductors,<sup>[11,21–23]</sup> low-dimensional materials,<sup>[19,24,25]</sup> phase transition materials,<sup>[18,26–31]</sup> and field

optimizing structures like cavities,<sup>[18,27]</sup> metasurfaces,<sup>[21,26,30]</sup> and quantum wells<sup>[11,22,23]</sup> are being utilized.


Compared to spectral control, spatially resolved control of thermal emission is much more challenging yet crucial for information applications, such as thermal camouflage,<sup>[19]</sup> combat identification,<sup>[32]</sup> and IR target simulation.<sup>[33]</sup> Passive metal metasurfaces can achieve switchable spatially resolved modulation of thermal emission by spatially arranging units with different emission properties but can hardly be dynamically reconfigured owing to the fixed geometric parameters.<sup>[34,35]</sup> In addition, microelectromechanical-system-based IR emitter arrays or digital mirror devices can achieve spatially resolved thermal emission control but require electrical, thermal, or mechanical actuators to independently control each pixel, increasing the manufacturing complexity.<sup>[32,36,37]</sup> Moreover, a transducer consisting of a metallic black on a thin polymer substrate can convert a visible image into an IR image through localized optical heating and thermal emission.<sup>[38]</sup> Similarly, active metasurfaces incorporating a photosensitive ZnO layer can be used to spatially modulate the emissivity by optically controlling the carrier concentrations with masks; however, such devices exhibit a low dynamic range of the emissivity modulation ( $\approx 0.12$  in the 7.5–14 μm wavelength range).<sup>[21]</sup> Therefore, spatially resolved dynamically reconfigurable control of thermal emission for practical applications remains elusive.

Z. Xu, Prof. Q. Li, Dr. K. Du, H. Luo, H. Zhu, Dr. P. Ghosh, Prof. W. Shen  
State Key Laboratory of Modern Optical Instrumentation  
College of Optical Science and Engineering  
Zhejiang University  
Hangzhou 310027, China  
E-mail: qiangli@zju.edu.cn

Dr. S. Long, Y. Yang, Dr. X. Cao  
State Key Laboratory of High Performance Ceramics and Superfine  
Microstructure  
Shanghai Institute of Ceramics  
Chinese Academy of Sciences  
Shanghai 200050 China

Prof. M. Qiu  
Key Laboratory of 3D Micro/Nano Fabrication and Characterization of  
Zhejiang Province  
School of Engineering  
Westlake University  
18 Shilongshan Road Hangzhou 310024, China

Prof. M. Qiu  
Institute of Advanced Technology  
Westlake Institute for Advanced Study  
18 Shilongshan Road Hangzhou 310024, China

 The ORCID identification number(s) for the author(s) of this article can be found under <https://doi.org/10.1002/lpor.201900162>

DOI: 10.1002/lpor.201900162

Here, we report a spatially resolved and dynamically reconfigurable thermal emission control platform. A light stimulated phase transition enables the spatial control of thermal emission. Meanwhile, hysteresis in the phase transition process of VO<sub>2</sub> is further explored to obtain up to nine emissivity levels with the same device. In addition, the planar cavity structured device extends the working wavelength range to the entire second atmosphere transparent window (8–14 μm), while the dynamic range of the average emissivity remains large (6.8 dB, 0.19–0.91).

## 2. Experimental Section

### 2.1. Calculation and Simulation

The transfer matrix method was used to calculate the electric field distribution and optical absorptance inside the device. In the calculation, the refractive indices of VO<sub>2</sub> were derived from refs. [39,40]. The refractive indices of the other materials used in calculation are available in Sections S1 and S2, Supporting Information. To obtain the maximum temperature that the VO<sub>2</sub> film could achieve under the illumination of a laser beam, light-induced heating was calculated with the solid heat transfer module of COMSOL Multiphysics. In the heat simulation, the absorption rate along the depth direction of the device was used to define the heat source. Meanwhile, the lateral electric field distribution was defined as a Gaussian distribution to model the Gaussian laser beam. The heat transfer coefficient, heat conductivity, and heat capacity of the materials used in the simulation are available in Section S3, Supporting Information.

### 2.2. Fabrication of the Device

{Au} was thermally evaporated onto a single-side polished and undoped silicon substrate. ZnS and TiO<sub>2</sub> were electrically evaporated. TiO<sub>2</sub> was deposited below and on top of the ZnS layer as barrier layers to protect the ZnS at high temperatures. The VO<sub>2</sub> layer was fabricated by combining a reactive magnetron sputtering system and a postannealing process. V<sub>2</sub>O<sub>3</sub> (99.95%) targets (diameter of 4 inches) were used for the fabrication of VO<sub>2</sub> and the deposition procedure was carried out using an integrated lock-load system. An initial pump-down process was executed to reach the original pressure of 5.0 × 10<sup>-4</sup> Pa for the deposition chamber. Then, {Ar} (99.99% pure) gas and {Ar} (97%) and O<sub>2</sub> (3%) mixed gases (99.99% pure) with an {Ar}/({Ar}+O<sub>2</sub>) proportion of 4.0 were introduced into the atmosphere, while the pressure of the chamber was maintained at 6 mTorr when the total gas flow was approximately 50 sccm. Sputtering then took place at a power of 200 W to deposit the amorphous VO<sub>x</sub>. Finally, a postannealing process was carried out at 430 °C and ≈6 Torr for 5 min in a vacuum furnace to obtain the VO<sub>2</sub>.

### 2.3. Thermal Patterning

The laser source for patterning was a 405 nm continuous wave (CW) laser diode module. The “ON” and “OFF” states of the laser were controlled by a gate voltage. The modulation rate of the laser was 1 kHz. This laser was mounted on an X–Y positioning system

driven by stepper motors. The average laser power was controlled by the duty cycle (the output duration in each period, see Section S3, Supporting Information). In binary patterning (bilevel emissivity control), the duty cycles were set to 0% and 100% for low- and high-emissivity patterning, respectively. In grayscale patterning (multilevel emissivity control), the duty cycles were set between 0% and 100% depending on the grayscale value of each pixel. The heating stage was maintained at 67 °C during the writing process.

### 2.4. Emissivity Measurement

Measurements of the thermal emissivity were performed with a Fourier transform infrared (FTIR) spectrometer (Bruker Vertex 70) with a deuterated lanthanum- $\alpha$ -alanine doped triglycine sulfate (DTGS) detector. In the measurement, references were indispensable to obtain the absorptance / emissivity. In the mid-IR range, a wafer coated by an optically thick gold layer could be regarded as a total reflector whose reflectance is unity. A gold-coated wafer was baked on a candle flame for 5 min to deposit black soot. Such black soot was expected to have a wavelength-independent emissivity value between 0.95 and 0.98 in the mid-IR range<sup>[28,41]</sup> and the emissivity of the black soot was assumed to be 0.96 in this work. During the measurements, the devices and black-body references were mounted on a computer-controlled heating stage (Bruker A540 emittance adaptor). In the experiment, the thermal emission spectra of the samples and black-body references were measured for various temperatures as  $I_s(\lambda, T)$  and  $I_{BB}(\lambda, T)$ , respectively. The emissivity  $\epsilon_s(\lambda, T)$  of the device was calculated by  $\epsilon_s = I_s(\lambda, T)/I_{BB}(\lambda, T)$ . For the average emissivity in the wavelength range of 8–14 μm,  $\epsilon_{avg}(T)$  was calculated using Equation (1)

$$\epsilon_{avg}(T) = \frac{\int_{8 \mu\text{m}}^{14 \mu\text{m}} \epsilon_s(\lambda, T) \frac{2\pi hc_0^2}{\lambda^5 \left[ \exp\left(\frac{hc_0}{\lambda k_B T}\right) - 1 \right]} d\lambda}{\int_{8 \mu\text{m}}^{14 \mu\text{m}} \frac{2\pi hc_0^2}{\lambda^5 \left[ \exp\left(\frac{hc_0}{\lambda k_B T}\right) - 1 \right]} d\lambda} \quad (1)$$

### 2.5. Thermal Emission Characterization

A thermal camera (FLIR S65, resolution of 320 × 240) was used for the characterization of the spatially resolved multilevel control (Figure 4). For a 60° oblique view, a 36-mm wide-angle IR lens was mounted for large-area imaging. For a normal view, an extra close-up lens was mounted for close imaging with a higher resolution. A spot thermal camera (FLIR TG165, resolution of 80 × 60) is used for the characterization of the thermal emission during the heating and cooling processes (Figure 2c).

## 3. Simulation and Experimental Results

### 3.1. Thermal-Photonic Device with Switchable Emissivity States

The combination of a reversible phase transition material and a field optimization structure provides a simplified but efficient

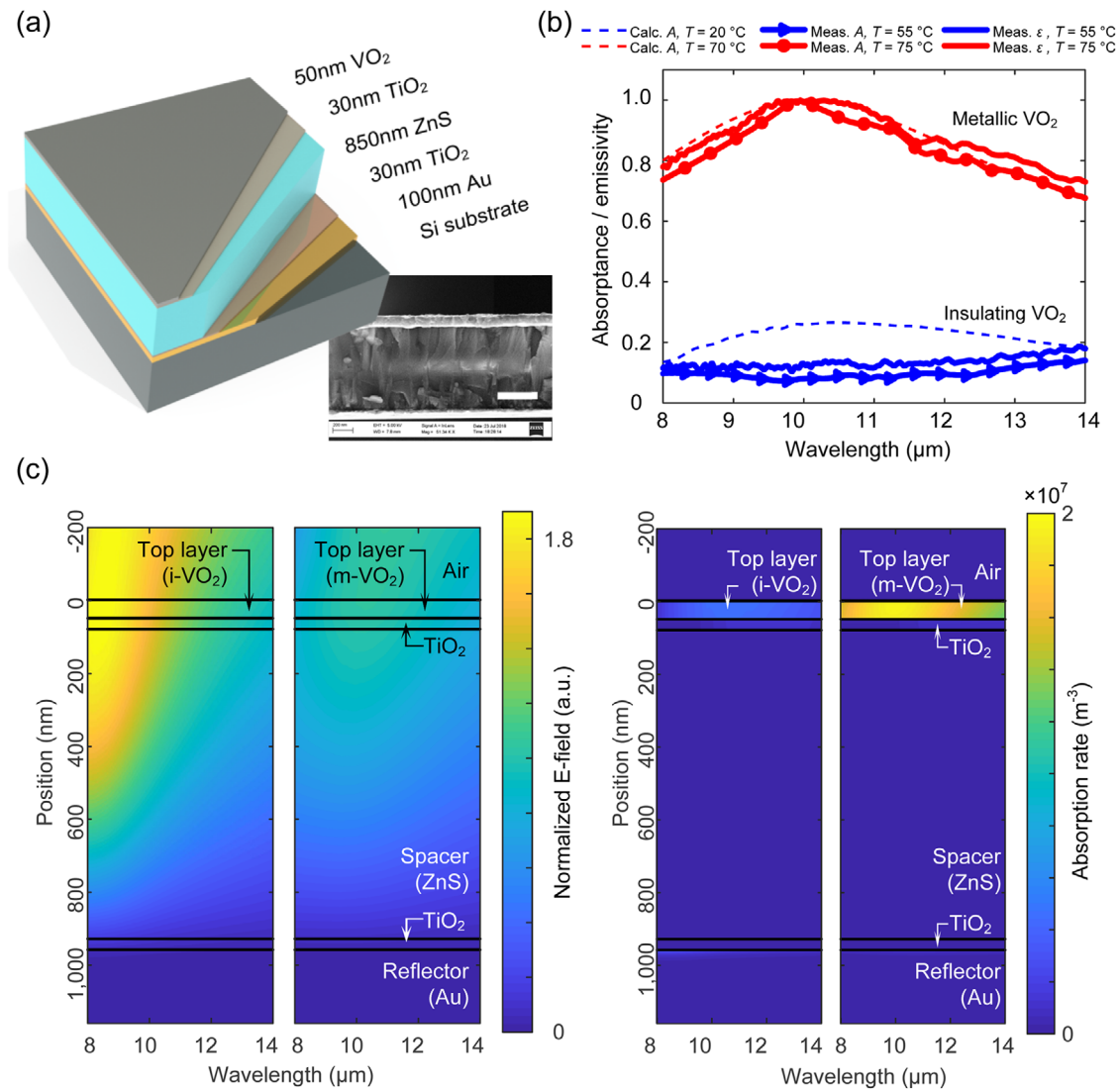


**Figure 1.** Reconfigurable thermal photonic device. a) Schematic and a scanning electron microscopy (SEM) image of the cross section of the device. The scale bar is 400 nm. b) Measured absorbance (solid lines with marks)/emissivity (solid lines) and calculated absorbance (dashed line) in the mid-IR region. The red and blue lines correspond to metallic and insulating VO<sub>2</sub>, respectively. c) Calculated normalized electric field distribution (left) and volume absorption rate (right) for normal plan wave incidence. The high- and low-emissivity states of the device correspond to metallic and insulating VO<sub>2</sub>, respectively.

way to realize emissivity switching, which also exhibits reconfigurability and a large contrast between the two states. The structure of the device is illustrated in **Figure 1a**. The inclusion of the VO<sub>2</sub> material with a phase transition is of vital importance for dynamically reconfigurable thermal emission control because it exhibits an apparent change in the complex refractive index [39,40] during the phase transition in the mid-IR wavelength range. This phase transition can also be reversed under certain conditions. The adoption of a photonic structure planarized with field optimization guarantees the maximization of the emissivity dynamic range, while the fabrication process remains simple. The whole planarized structure consists of a VO<sub>2</sub> top layer, a lossless spacer (TiO<sub>2</sub>/ZnS/TiO<sub>2</sub>), and a highly reflective bottom metal layer (Au). The VO<sub>2</sub> layer is placed on the top of the spacer layer to maximize the overall absorption/emission in the

8–14 μm atmospheric window when VO<sub>2</sub> is in the metallic phase. The lossless spacer together with the highly reflective Au layer can minimize the absorption/emission when VO<sub>2</sub> is in the insulating phase to ensure a large dynamic range of the emissivity modulation. In the fabrication process, the amorphous VO<sub>x</sub> is first sputtered with V<sub>2</sub>O<sub>3</sub> targets and subsequently postannealed in O<sub>2</sub>/[Ar] atmosphere to form VO<sub>2</sub> (see Section 2.2 for more details). The two TiO<sub>2</sub> layers act as protection layers to avoid the decomposition or oxidization of the ZnS layer.<sup>[42]</sup> The thickness of each layer, which is optimized for a large contrast in the emissivity between the two phases of VO<sub>2</sub> (insulating and metallic phases, which are termed insulating VO<sub>2</sub> and metallic VO<sub>2</sub>, respectively), is 50 nm / 30 nm / 850 nm / 30 nm / 100 nm from top to bottom (see Section S1, Supporting Information).

The absorptance and emissivity spectra of the thermal emitter for both the insulating VO<sub>2</sub> and metallic VO<sub>2</sub> phases are calculated with the transfer matrix method<sup>[43]</sup> and measured by an FTIR spectrometer (Figure 1b). The measured absorptance and emissivity agree well with each other as predicted by Kirchhoff's law of thermal radiation. The difference between the calculated absorptance and measured absorptance/emissivity for the insulating VO<sub>2</sub> device can be attributed to the temperature difference (20 °C for the insulating VO<sub>2</sub> parameters used in the calculation and 55 °C for the experiment, which is chosen for a better signal-to-noise ratio in the thermal emission measurement). During the insulator-to-metal transition of VO<sub>2</sub>, the average emissivity of the device in the second atmospheric window (8–14 μm) increases drastically from 0.19 to 0.91. Meanwhile, the peak emissivity reaches ≈1 at a wavelength of 10 μm for metallic VO<sub>2</sub>.

To unveil the physics behind this sharp contrast in the emissivity between the insulating VO<sub>2</sub> and metallic VO<sub>2</sub> samples, the normalized electric field distribution, volume absorption rate (Figure 1c), and specific absorptivity in each layer (Figure S3c, Supporting Information) are further investigated. The electric fields are quite weak at the Au surface because of the π-phase shift corresponding to reflection. Due to the existence of an approximately λ/4n-thick spacer layer, the electric fields are enhanced in the VO<sub>2</sub> layer in both phases. Due to the resistive loss in the layered structure, the power dissipation density along the normal direction (W m<sup>-3</sup>) can be expressed as <sup>[44,45]</sup>

$$w(z) = 1/2\omega\epsilon_0\epsilon_r''|\mathbf{E}(z)|^2 \quad (2)$$

where ω, ε<sub>0</sub>, and ε<sub>r</sub>'' are the angular frequency of the incident light, vacuum permittivity, and imaginary part of the relative complex permittivity, respectively. By normalizing this power dissipation density with respect to the time-averaged incident energy flow, the optical absorbance is derived as

$$\alpha(z) = \frac{w(z)}{\langle \mathbf{E} \times \mathbf{H} \rangle} = Z_0\omega\epsilon_0\epsilon_r'' \left| \frac{\mathbf{E}(z)}{E_0} \right|^2 \quad (3)$$

where Z<sub>0</sub> = |E|/|H| is the impedance of free space and E<sub>0</sub> is the amplitude of the incident electric field in the calculation. The device exhibits a much lower volume absorption rate with low-loss insulating VO<sub>2</sub> than with lossy metallic VO<sub>2</sub>. Most of the absorption occurs in the VO<sub>2</sub> layer for both the insulating and metallic phases (97.7% and 80.7% at λ = 10 μm, respectively, see Section S1, Supporting Information). With the increase in optical loss during the insulator-to-metal phase transition, an ≈4.5-fold increase in the volume absorption rate in the VO<sub>2</sub> layer is expected according to the calculation (Figure S1c, Supporting Information), which is in good agreement with the measured emissivity. As shown by the calculated absorptance and measured emissivity, this thermal photonic device can guarantee a large dynamic range of emissivity control.

### 3.2. Multilevel Thermal Emission Control with Phase Transition Hysteresis

In addition to low- and high-emissivity states, the intermediate states<sup>[46]</sup> and the dynamic process of phase-transition-related

phenomena also have great significance for achieving multilevel and reconfigurable thermal emission control. The emissivity of the device is further measured for both the heating and cooling processes between 40 °C and 100 °C (Figure 2a). At low temperatures (≤ 53 °C), VO<sub>2</sub> is in the insulating phase, and the device exhibits a low emissivity across the measured spectral range. In contrast, a high emissivity can be obtained at high temperatures (≥ 79 °C), where VO<sub>2</sub> is in the metallic phase. In particular, the maximum emissivity approaches unity at a wavelength of 10 μm at high temperatures (black dashed lines in Figure 2a). The emissivity changes drastically during the heating (from 69 °C to 80 °C) and cooling (from 80 °C to 53 °C) processes, where the insulator-to-metal and metal-to-insulator phase transitions of VO<sub>2</sub> occur, respectively. From the derived average emissivity in the 8–14 μm wavelength range at different temperatures (40–90 °C) (Figure 2b), hysteresis in the temperature dependent emissivity during the heating and cooling progress can be explicitly observed. This hysteresis behavior is similar to that for other parameters (e.g., the sheet resistance and transmittance<sup>[47]</sup>) during the phase transition in VO<sub>2</sub>. Due to this hysteresis, two emissivity states corresponding to the two VO<sub>2</sub> phases are allowed at a fixed temperature in the hysteresis region (shaded area in Figure 2b).

The hysteresis behavior provides an avenue for attaining bilevel emissivity control through a specific temperature control path. For instance, the device first shows a low average emissivity for insulating VO<sub>2</sub> at T<sub>1</sub> = 53 °C (state I<sub>1</sub> in Figure 2b, ε<sub>1</sub> = 0.16). When the device is heated to T<sub>2</sub> = 69 °C, the average emissivity increases slightly (state I<sub>2</sub> in Figure 2b, ε<sub>2</sub> = 0.20), and the insulator-to-metal phase transition of VO<sub>2</sub> is just initiated. Once the device is further heated to T<sub>3</sub> = 80 °C, the emissivity rapidly increases to a higher value (state M<sub>1</sub> in Figure 2b, ε<sub>3</sub> = 0.90), indicating the metallization of the VO<sub>2</sub> layer. At the beginning of the cooling process, the average emissivity remains at a higher value even when the temperature is decreased to T<sub>4</sub> = T<sub>2</sub> = 69 °C (state M<sub>2</sub> in Figure 2b, ε<sub>4</sub> = 0.89), indicating that the VO<sub>2</sub> remains in the metallic phase. In this way, T<sub>1</sub> and T<sub>3</sub> can be regarded as the lower and upper temperature limits that allow bilevel control of the emissivity at a fixed temperature. Thermal images of the device (for states I<sub>1</sub>, I<sub>2</sub>, M<sub>1</sub>, and M<sub>2</sub>) and the black soot are recorded (Figure 2c). At the same temperature (T<sub>2</sub> = T<sub>4</sub> = 69 °C), the thermal emission intensity of the device for metallic VO<sub>2</sub> (M<sub>2</sub>) is close to that of the black-body reference, while the thermal emission intensity for insulating VO<sub>2</sub> (I<sub>2</sub>) is close to that of the metallic background (aluminum heat plate) with a low emissivity.

In addition to bilevel control of the emissivity, multilevel control can be achieved with multiple phase transition hysteresis via a specific temperature control path. The aforementioned temperature range for the hysteresis loop is between T<sub>1</sub> (= 53 °C) and T<sub>3</sub> (= 80 °C), where VO<sub>2</sub> is in the insulating and metallic phases, respectively. By controlling the peak temperature (T<sub>p</sub>) in the heating process below T<sub>3</sub> (=80 °C), intermediate states (an emissivity between ε<sub>2</sub> and ε<sub>4</sub>) at temperature T<sub>2</sub> can be obtained. To confirm the existence of such intermediate states at temperature T<sub>2</sub>, the thermal emission intensity and emissivity of the device in different hysteresis loops are measured by controlling the peak temperature T<sub>p</sub> (72 °C, 74 °C, 76 °C, 78 °C, and 100 °C) in different heating-cooling loops. From the averaged thermal emission intensity and emissivity in the 8–14 μm wavelength range

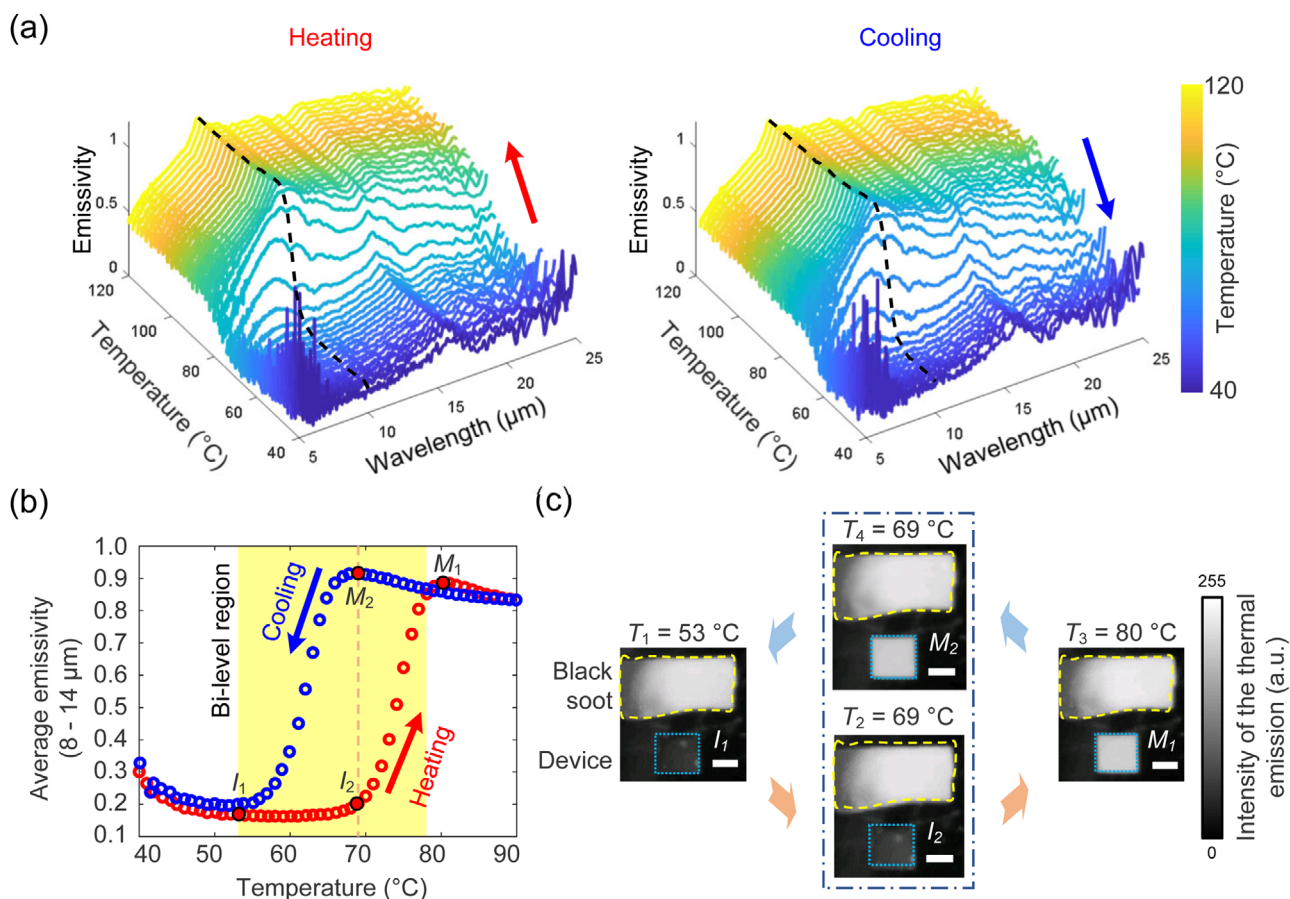


**Figure 2.** Temperature-based thermal emission control. a) Measured temperature-dependent emissivity spectra during the (left) heating and (right) cooling processes. The emissivities at a wavelength of 10  $\mu\text{m}$  are marked with dashed lines. b) Measured temperature-dependent average emissivity (8–14  $\mu\text{m}$ ) during the heating and cooling processes. The red and blue marks correspond to the data points collected during the heating and cooling processes, respectively. The shaded region indicates the temperature range that allows two different emissivities at a same temperature. The solid disks in red represent the emissivity states  $I_1$ ,  $I_2$ ,  $M_1$ , and  $M_2$  during the heating and cooling processes. c) Thermal images of the device and the black soot reference for states  $I_1$ ,  $I_2$ ,  $M_1$ , and  $M_2$ . Two thermal emission states, a high-emissivity state ( $M_2$ ) and a low-emissivity state ( $I_2$ ), can be obtained for the device at the same temperature ( $T_2 = T_4 = 69$  °C). The scale bar is 5 mm.

(Figure 3a,b), six different levels can be distinguished from the five hysteresis loops in the phase transition region. For example, at  $T_2$  (= 69 °C), six average emissivity states (0.19, 0.38, 0.55, 0.72, 0.81, and 0.91) corresponding to different temperature control paths can be obtained. Therefore, these controllable phase transition hysteresis loops enable multilevel control of the emissivity at one temperature, thus providing the possibility for spatially resolved multilevel emissivity control.

### 3.3. Spatially Resolved Multilevel Thermal Emission Control

Spatially resolved dynamically reconfigurable control of the thermal emission with phase transition hysteresis is demonstrated with an optically controllable platform. The light-induced heating generated with the laser writing system allows spatial control of the localized temperature via control of the incident energy. Accordingly, the intermediate states in the phase transition hysteresis of  $\text{VO}_2$  can be spatially controlled, enabling spatially resolved

control of the thermal emission. A schematic of the experimental system for spatially resolved dynamically reconfigurable emission control is shown in Figure 4a. The whole system consists of a heating stage for temperature control, a thermal camera for thermal imaging, a gate controlled laser for light-induced heating, and moving arms for positioning. In the experiment, a 405 nm wavelength laser diode is chosen as the laser source ( $\approx 70\%$  absorption by the device at this wavelength, see Section S2, Supporting Information). The temperature of the heating stage is set to 68 °C as a temperature bias to obtain a large dynamic range of emissivity control. The peak temperature of  $\text{VO}_2$  is tuned with laser pulses with different durations. The spatially resolved thermal emission control is recorded with a focal-plane array thermal camera with a spectral response range of 8–14  $\mu\text{m}$ . An oblique view ( $\approx 60^\circ$ ) is chosen for the thermal camera, because the normal view is blocked by the laser module during the writing process. The normal view is only used during the erasing process.

A binary pattern (the logo of Zhejiang University) is written to demonstrate the bilevel thermal emission control. The corresponding binary digital mask (inset of Figure 4 b–i) is used to

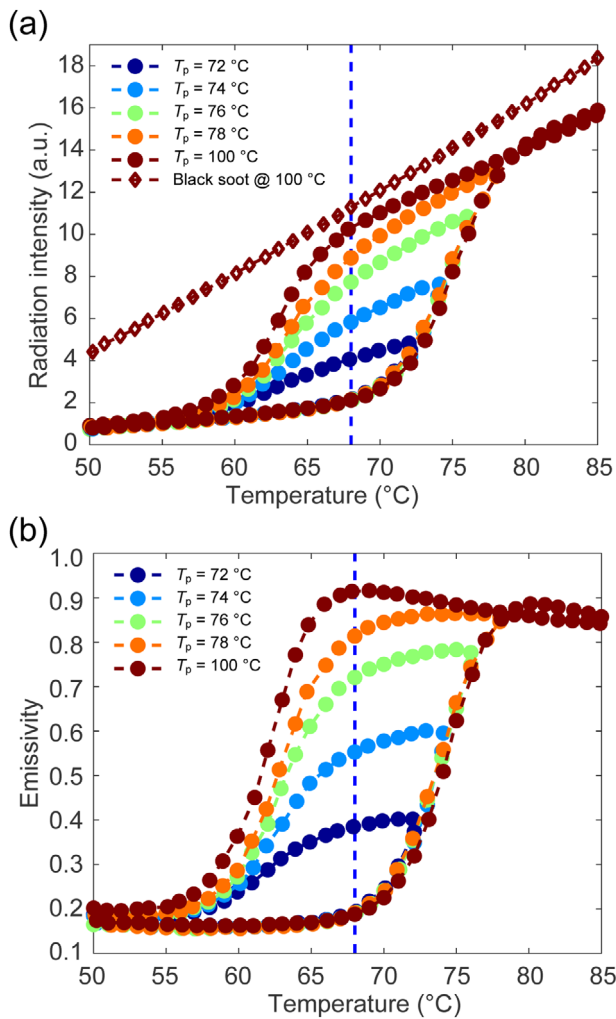


**Figure 3.** Control of multilevel thermal emission. a) Measured temperature-dependent average radiation intensity (8–14  $\mu\text{m}$ ) of the device and the black soot reference. Multiple phase transition hysteresis loops are realized with different peak temperatures  $T_p$  (72  $^{\circ}\text{C}$ , 74  $^{\circ}\text{C}$ , 76  $^{\circ}\text{C}$ , 78  $^{\circ}\text{C}$ , and 100  $^{\circ}\text{C}$ ). b) Measured temperature-dependent average emissivity (8–14  $\mu\text{m}$ ) of the device.

switch the laser output so that the  $\text{VO}_2$  phase transition can be triggered by the laser illumination. The thermal images of the pattern (Figure 4 b-ii, b-iv, normal and oblique views, respectively) clearly demonstrate spatially resolved thermal emission. The radiant temperature  $T_r$ , which is derived from the thermal image, can be used to quantify the emission intensity. From the extracted radiant temperature increase ( $\Delta T_r$ ) after the patterning (Figure 4 b-iii), a maximum increase of 7  $^{\circ}\text{C}$  is obtained, demonstrating an enhanced thermal emissivity after the patterning. When the device is removed from the heating stage to allow natural cooling, the thermal patterns fade away in  $\approx 9$  s, during which the  $\text{VO}_2$  returns to the insulating phase (Figure 4 b-iv to -vi, see Videos S1 and S2, Supporting Information). The erased patterns do not appear even if the device is placed back on the heating stage.

Grayscale patterns (a checkerboard pattern and “panda” images) are further written to demonstrate multilevel thermal emission control. As demonstrated above, the multiple levels of the

thermal emissivity require control of the peak temperature  $T_p$  in different hysteresis loops. However, the duration of the laser pulse is tuned to control the peak temperature  $T_p$  of  $\text{VO}_2$  (see Section S3, Supporting Information). For the checkerboard pattern (Figure 4c), each row of squares is written by laser pulses with different durations defined by the grayscale pattern (inset of Figure 4c). The patterned squares among different rows display different radiation temperatures ( $T_r$ ). To quantitatively characterize the multilevel emission control, the mean and standard deviation values of  $T_r$  of the patterned squares in the same row are extracted and analyzed. A comparison among different rows demonstrates nine-level thermal emission control (Figure 4c). For the “panda” thermal image (Figure 4d), the device vividly reproduces the original image (inset of Figure 4d), demonstrating the flexibility of this platform for spatially resolved multilevel emission control. The viewing angle is large for the thermal images of this thermal photonic device. The thermal “panda” image remains distinguishable for various viewing angles ( $\theta = 0^{\circ}$ ,  $30^{\circ}$ , and  $60^{\circ}$ ) (Figure 4d). It is also noted that all three patterns (the logo of Zhejiang University, the checkerboard pattern and the “panda” images) are written and characterized on the same sample sequentially and no apparent performance degradation in the emissivity modulation is observed, which demonstrates the stability in terms of repeated cycling for the material/device in this platform. (see Section S4, Supporting Information).

#### 4. Discussion and Conclusion

Several issues related to the material and device/system performance of this platform are discussed as follows. 1) Regarding the temperature for the maximum range of the emissivity modulation and the temperature range for the multilevel modulation, the former is primarily determined by the phase transition temperature, while the latter is mainly determined by the temperature range in which the phase transition hysteresis occurs. The device in this work exhibits a phase transition hysteresis loop that is 15  $^{\circ}\text{C}$  in width and centered at 68  $^{\circ}\text{C}$ . The width of the phase transition hysteresis loop can be engineered from  $\approx 3^{\circ}\text{C}$  to  $\approx 30^{\circ}\text{C}$  by controlling the  $\text{VO}_2$  deposition conditions<sup>[48]</sup> or adjusting the buffer layers,<sup>[49]</sup> while the phase transition temperature can also be varied from  $\approx 20^{\circ}\text{C}$  to  $\approx 70^{\circ}\text{C}$  by defect engineering in the  $\text{VO}_2$  layer.<sup>[50]</sup> More flexibility in the working temperature could be possible by employing a specific modification in the deposited  $\text{VO}_2$  layer. 2) Regarding the writing and erasing speeds, the videos provided in the Supporting Information show that the patterns are written with a line speed of  $\approx 10.8$   $\text{mm s}^{-1}$  and erased in  $\approx 9$  s. Since the phase transition response of  $\text{VO}_2$  is less than a picosecond,<sup>[51]</sup> the bottlenecks of the operating speed in this system are the slow positioning speed during the writing process and the slow natural heat conduction and convection during the erasing process. The temporal responses of this platform could be optimized with a high-performance positioning system and augmented cooling conditions. 3) Regarding the spatial resolution, the demonstrated feature size in the spatial patterning is 400  $\mu\text{m}$  (the linewidth of the Zhejiang University logo in Figure 4b), which can be considerably reduced with dedicated focusing and positioning. 4) Regarding the overall contrast ratio, for

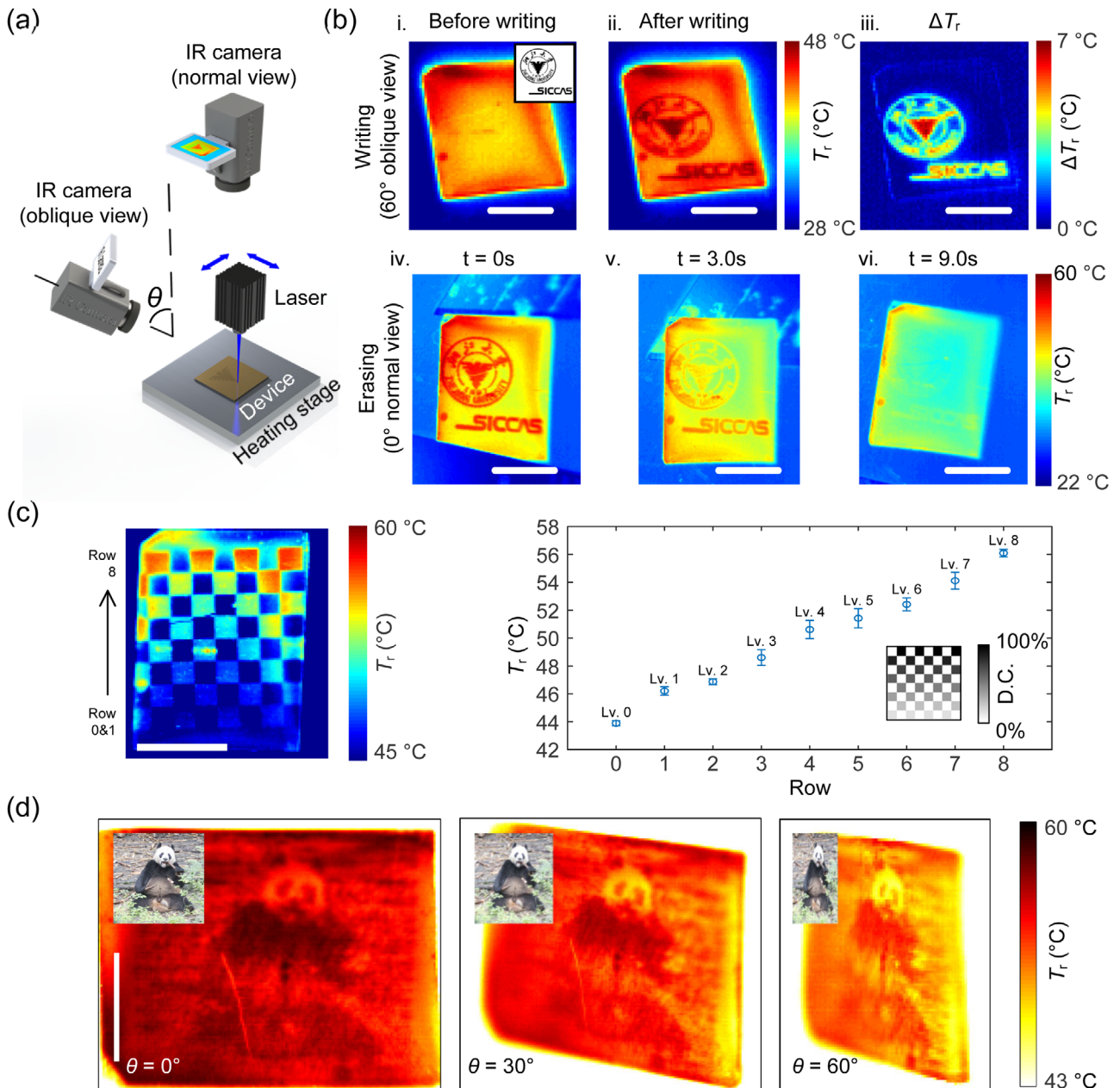


**Figure 4.** Multilevel thermal emission control. a) Schematic of the spatially resolved thermal emission control platform. b) i)–iii) Writing and iv)–vi) erasing of the bilevel thermal images (Zhejiang University logo; reproduced with permission, copyright Zhejiang University). i)–iii) are the thermal images before and after writing and the change in the radiant temperature, respectively. c) Multilevel thermal emission control with phase transition hysteresis. Different rows in the checkerboard are written by 1 kHz laser pulses with different duty cycles (defined by the grayscale pattern, inset of Figure 4c). The mean and standard deviation values of the radiation temperatures of the patterned squares in the same row are extracted, demonstrating nine-level thermal emission control. d) Multilevel thermal “panda” images for different viewing angles ( $\theta = 0^\circ$ ,  $30^\circ$ , and  $60^\circ$ ). The scale bars are 1 cm.

the low-emissivity state, low-loss mirrors such as dielectric thin film stacks can be used to minimize the emissivity.

In summary, a new type of spatially resolved dynamically reconfigurable thermal emission control platform, which consist of a  $\text{VO}_2$  material with phase transition hysteresis, a planarized thermal photonic structure with field optimization, and an optically controllable patterning system, is developed and validated in this work. This type of control of thermal patterns retains

many key capabilities of optical patterns, yet the spatially resolved dynamically reconfigurable emitters are, in principle, different from passive reflective/transmissive devices.<sup>[52]</sup> The thermal patterns are active radiation sources that obey the Stefan–Boltzmann law, so an external light source is not required. In addition, the presented systems feature state-of-the-art spatially resolved thermal emission control technologies. Moreover, the materials and devices in this platform have been intrinsically designed for high

reconfigurability and simple manufacturability. Therefore, this spatially resolved dynamically reconfigurable thermal emission control platform may facilitate information-related applications such as IR camouflage and thermal data storage and is expected to stimulate new possibilities for modern thermal management technologies toward an energy-efficient future.

## Supporting Information

Supporting Information is available from the Wiley Online Library or from the author.

## Acknowledgements

This work is supported by National Key Research and Development Program of China (2017YFE0100200 and 2017YFA0205700), National Natural Science Foundation of China (Grant Nos. 61575177, 61425023, and 61775194), the Fundamental Research Funds for the Central Universities, the Youth Innovation Promotion Association, Chinese Academy of Sciences (No. 2018288), and the Shanghai Pujiang Program (No. 18PJ051).

## Conflict of Interest

The authors declare no conflict of interest.

## Keywords

phase transition hysteresis, spatially resolved, thermal emission control

Received: May 13, 2019

Revised: September 25, 2019

Published online: December 10, 2019

- [1] A. P. Raman, M. A. Anoma, L. Zhu, E. Rephaeli, S. Fan, *Nature* **2014**, 515, 540.
- [2] P. C. Hsu, C. Liu, A. Y. Song, Z. Zhang, Y. Peng, J. Xie, K. Liu, C. L. Wu, P. B. Catrysse, L. Cai, S. Zhai, A. Majumdar, S. Fan, Y. Cui, *Sci. Adv.* **2017**, 3, e1700895.
- [3] J. Mandal, Y. Fu, A. C. Overvig, M. Jia, K. Sun, N. N. Shi, H. Zhou, X. Xiao, N. Yu, Y. Yang, *Science* **2018**, 362, 315.
- [4] Y. Zhai, Y. Ma, S. N. David, D. Zhao, R. Lou, G. Tan, R. Yang, X. Yin, *Science* **2017**, 355, 1062.
- [5] H. Luo, Q. Li, K. Du, Z. Xu, H. Zhu, D. Liu, L. Cai, P. Ghosh, M. Qiu, *Nano Energy* **2019**, 65, 103998.
- [6] J. Zhou, X. Chen, L. J. Guo, *Adv. Mater.* **2016**, 28, 3017.
- [7] T. Yokoyama, T. D. Dao, K. Chen, S. Ishii, R. P. Sugavaneshwar, M. Kitajima, T. Nagao, *Adv. Opt. Mater.* **2016**, 4, 1987.
- [8] A. Lenert, D. M. Bierman, Y. Nam, W. R. Chan, I. Celanovic, M. Sol-jacic, E. N. Wang, *Nat. Nanotechnol.* **2014**, 9, 126.
- [9] H. T. Miyazaki, T. Kasaya, M. Iwanaga, B. Choi, Y. Sugimoto, K. Sakoda, *Appl. Phys. Lett.* **2014**, 105, 121107.
- [10] A. Lochbaum, Y. Fedoryshyn, A. Dorodnyy, U. Koch, C. Hafner, J. Leuthold, *ACS Photon.* **2017**, 4, 1371.
- [11] T. Inoue, M. De Zoysa, T. Asano, S. Noda, *Nat. Mater.* **2014**, 13, 928.
- [12] J. H. Park, S. E. Han, P. Nagpal, D. J. Norris, *ACS Photonics* **2016**, 3, 494.
- [13] O. Ilic, P. Bermel, G. Chen, J. D. Joannopoulos, I. Celanovic, M. Sol-jacic, *Nat. Nanotechnol.* **2016**, 11, 320.
- [14] B. Liu, W. Gong, B. Yu, P. Li, S. Shen, *Nano Lett.* **2017**, 17, 666.
- [15] E. Sakat, L. Wojszwyk, J. P. Hugonin, M. Besbes, C. Sauvan, J. J. Greffet, *Optica* **2018**, 5, 175.
- [16] J. J. Greffet, R. Carminati, K. Joulain, J. P. Mulet, S. Mainguy, Y. Chen, *Nature* **2002**, 416, 61.
- [17] L. Xiao, H. Ma, J. Liu, W. Zhao, Y. Jia, Q. Zhao, K. Liu, Y. Wu, Y. Wei, S. Fan, K. Jiang, *Nano Lett.* **2015**, 15, 8365.
- [18] Y. Qu, Q. Li, L. Cai, M. Pan, P. Ghosh, K. Du, M. Qiu, *Light Sci. Appl.* **2018**, 7, 26.
- [19] O. Salihoglu, H. B. Uzlu, O. Yakar, S. Aas, O. Balci, N. Kakenov, S. Balci, S. Olcum, S. Suzer, C. Kocabas, *Nano Lett.* **2018**, 18, 4541.
- [20] X. Xie, X. Li, M. B. Pu, X. L. Ma, K. P. Liu, Y. H. Guo, X. G. Luo, *Adv. Funct. Mater.* **2018**, 28, 1706673.
- [21] Z. J. Coppens, J. G. Valentine, *Adv. Mater.* **2017**, 29, 1701275.
- [22] M. De Zoysa, T. Asano, K. Mochizuki, A. Oskooi, T. Inoue, S. Noda, *Nat. Photon.* **2012**, 6, 535.
- [23] S. Vassant, I. Moldovan Doyen, F. Marquier, F. Pardo, U. Gennser, A. Cavanna, J. L. Pelouard, J. J. Greffet, *Appl. Phys. Lett.* **2013**, 102, 081125.
- [24] Y. Miyoshi, Y. Fukazawa, Y. Amasaka, R. Reckmann, T. Yokoi, K. Ishida, K. Kawahara, H. Ago, H. Maki, *Nat. Commun.* **2018**, 9, 1279.
- [25] Q. Li, J. Lu, P. Gupta, M. Qiu, *Adv. Opt. Mater.* **2019**, 7, 1900595.
- [26] A. Tittel, A. K. Michel, M. Schaferling, X. Yin, B. Gholipour, L. Cui, M. Wuttig, T. Taubner, F. Neubrech, H. Giessen, *Adv. Mater.* **2015**, 27, 4597.
- [27] K. Du, Q. Li, Y. Lyu, J. Ding, Y. Lu, Z. Cheng, M. Qiu, *Light Sci. Appl.* **2017**, 6, e16194.
- [28] M. A. Kats, R. Blanchard, S. Zhang, P. Genevet, C. Ko, S. Ramanathan, F. Capasso, *Phys. Rev. X* **2013**, 3, 041004.
- [29] K. Dong, S. Hong, Y. Deng, H. Ma, J. Li, X. Wang, J. Yeo, L. Wang, S. Lou, K. B. Tom, K. Liu, Z. You, Y. Wei, C. P. Grigoropoulos, J. Yao, J. Wu, *Adv. Mater.* **2018**, 30, 1703878.
- [30] Z. Li, Y. Zhou, H. Qi, Q. Pan, Z. Zhang, N. N. Shi, M. Lu, A. Stein, C. Y. Li, S. Ramanathan, N. Yu, *Adv. Mater.* **2016**, 28, 9117.
- [31] K. Sauvet, L. Sauques, A. Rougier, *J. Phys. Chem. Solids* **2010**, 71, 696.
- [32] X. Liu, W. J. Padilla, *Optica* **2017**, 4, 430.
- [33] O. M. Williams, *Infrared Phys. Technol.* **1998**, 39, 473.
- [34] M. Makhsyan, P. Bouchon, J. Jaeck, J. L. Pelouard, R. Haïdar, *Appl. Phys. Lett.* **2015**, 107, 251103.
- [35] D. Franklin, S. Modak, A. Vázquez-Guardado, A. Safaei, D. Chanda, *Light Sci. Appl.* **2018**, 7, 93.
- [36] H. San, X. Chen, P. Xu, F. Li, M. Cheng, in *Infrared Technology and Applications XXXIV*, SPIE, Orlando, FL **2008**.
- [37] D. B. Beasley, M. Bender, J. Crosby, T. Messer, in *Emerging Digital Micromirror Device Based Systems and Applications*, SPIE, San Jose, CA **2009**.
- [38] V. T. Bly, *Opt. Eng.* **1982**, 21, 216079.
- [39] D. Shelton, *PhD Thesis*, University of Central Florida, Orlando, FL **2010**.
- [40] S. Cuffe, D. Li, Y. Zhou, F. J. Wong, J. A. Kurvits, S. Ramanathan, R. Zia, *Nat. Commun.* **2015**, 6, 8636.
- [41] N. Gao, H. Sun, D. Ewing, *Int. J. Heat Mass Transf.* **2003**, 46, 2557.
- [42] T. Maruyama, T. Kawaguchi, *Thin Solid Films* **1990**, 188, 323.
- [43] L. A. Pettersson, L. S. Roman, O. Inganäs, *J. Appl. Phys.* **1999**, 86, 487.
- [44] B. Zhao, J. Zhao, Z. Zhang, *Appl. Phys. Lett.* **2014**, 105, 031905.
- [45] W. Wang, Y. Qu, K. Du, S. Bai, J. Tian, M. Pan, H. Ye, M. Qiu, Q. Li, *Appl. Phys. Lett.* **2017**, 110, 101101.



- [46] M. Gurvitch, S. Luryi, A. Polyakov, A. Shabalov, *IEEE Trans. Nanotechnol.* **2010**, *9*, 647.
- [47] R. Lopez, T. E. Haynes, L. A. Boatner, L. C. Feldman, R. F. Haglund, *Phys. Rev. B* **2002**, *65*, 224113.
- [48] R. A. Aliev, V. N. Andreev, V. M. Kapralova, V. A. Klimov, A. I. Sobolev, E. B. Shadrin, *Phys. Solid State* **2006**, *48*, 929.
- [49] S. Long, X. Cao, G. Sun, N. Li, T. Chang, Z. Shao, P. Jin, *Appl. Surf. Sci.* **2018**, *441*, 764.
- [50] J. Rensberg, S. Zhang, Y. Zhou, A. S. McLeod, C. Schwarz, M. Goldflam, M. Liu, J. Kerbusch, R. Nawrodt, S. Ramanathan, D. N. Basov, F. Capasso, C. Ronning, M. A. Kats, *Nano Lett.* **2016**, *16*, 1050.
- [51] M. F. Jager, C. Ott, P. M. Kraus, C. J. Kaplan, W. Pouse, R. E. Marvel, R. F. Haglund, D. M. Neumark, S. R. Leone, *Proc. Natl. Acad. Sci. U.S.A.* **2017**, *114*, 9558.
- [52] E. M. Bu-Ali, *Master Thesis*, Texas Tech University, Lubbock, Texas **2016**.